



Publication Year	2023
Acceptance in OA	2025-02-26T10:32:49Z
Title	Volatile exposures on the 67P/Churyumov-Gerasimenko nucleus
Authors	Fornasier, S., Hoang, H. V., FULLE, Marco, Quirico, E., CIARNIELLO, Mauro
Publisher's version (DOI)	10.1051/0004-6361/202245614
Handle	http://hdl.handle.net/20.500.12386/36247
Journal	ASTRONOMY & ASTROPHYSICS
Volume	672

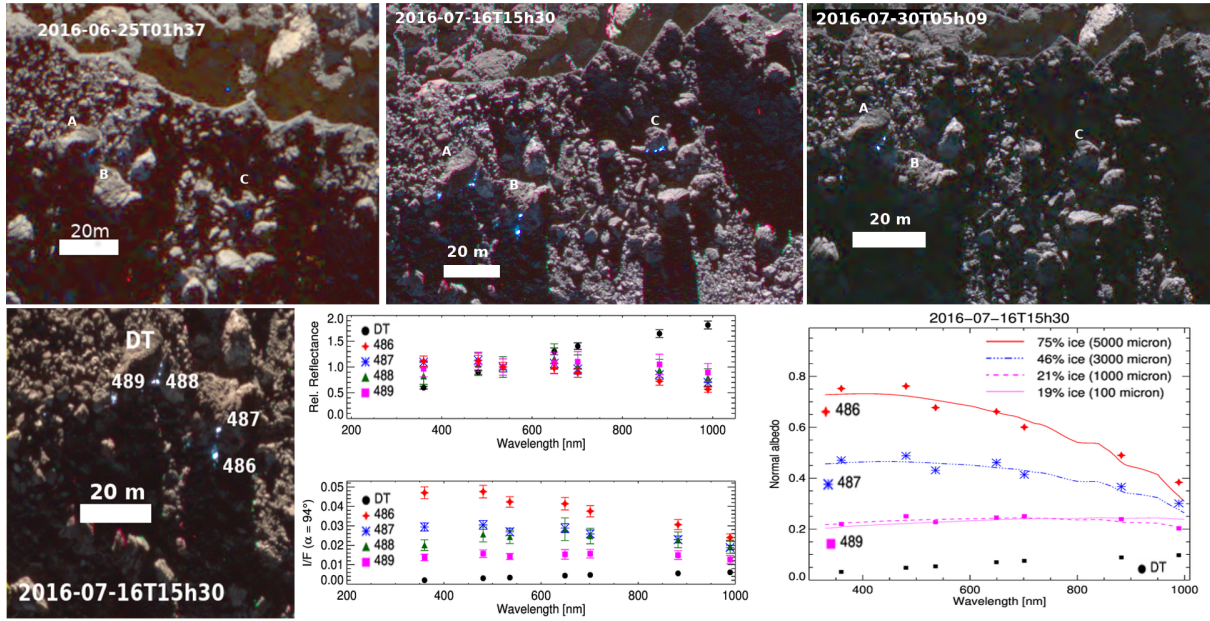


Fig. 8. Duration, spectrophotometry and compositional modeling of some blue bright spots in the Anhur region. Top: RGB images showing the blue BS observed in boulders named A, B, and C on 16 July 2016 (top central panel). This area is located close to the canyon-like structure of Anhur (Fornasier et al. 2017). Frosts and tiny blue spots were already present on 25 July 2016 images (top left panel) near the boulders named A and C, and a few close to boulder A were still visible in the 30 July 2016 images (top right panel). Bottom: relative reflectance and I/F of four selected blue BS located in the aforementioned A and B boulders: BS 486 (red star, slope = $-8.0\%/100\text{ nm}$), BS 487 (blue asterisk, slope = $-4.3\%/100\text{ nm}$), BS 488 (green triangle, slope = $-1.8\%/100\text{ nm}$), and BS 489 (magenta square, slope = $4.6\%/100\text{ nm}$) in Table A.1. DT indicates the cometary dark terrain. Bottom right: linear mixing models of the cometary dark terrain and water ice with different grain sizes reproducing the spectral behavior of the blue bright features. The estimated water ice abundance is indicated for the different models.

Khonsu are located). They were also detected in the small lobe (e.g., four BS in Wosret) and in the northern hemisphere (e.g., four BS each in the Babi and Seth regions), even if they are less frequent.

The evolution of the BS spectral slope toward smaller values in post-perihelion images is also confirmed in the analysis of the BS in individual regions, as shown in Table 2, where the slope systematically decreases in outbound orbits compared to the pre-perihelion images for regions observed during both periods and showing at least a few BS. It is worth noting that in Table 2 the spectral slope of the BS increased during the perihelion passage, while several studies reported a bluing of the comet colors (i.e., a decrease in the spectral slope) during the perihelion passage due to the seasonal cycle of water (Fornasier et al. 2016; Ciarniello et al. 2016, 2022). The higher spectral slope value of BS at perihelion is very likely an observational bias, due to the low spatial resolution of the data. In fact, BS are usually meter sized, thus during perihelion their spectral behavior is highly affected by the cometary red dark terrain, because BS are not resolved.

Most of the blue spots are located in shadowed areas, as shown in Fig. 8 or in Fornasier et al. (2021, their Fig. 10), and some others were found within frost fronts at the bottom of cliffs. The majority of the blue spots are only a few m^2 in size or even smaller, revealed thus in high-resolution images, while some other spots are a few tens of m^2 and the largest blue spot, with a surface of about 50 m^2 , is located in the Babi region (BS 395 in Table A.1). The estimated lifetime of the blue spots ranges from at least 20 minutes (BS 599) to nearly two weeks for BS 489 (Fig. 8).

The first bright blue spots we found in our analysis, and which motivated a deeper study, are located in the Anhur region

and were observed in high-resolution images acquired on 16 July 2016 when the comet was 3.4 au outbound, at a resolution of 0.19 m px^{-1} (Fig. 8). BS 486 and 487 in Table A.1 display a sharp decrease in the reflectance after 650 nm , with spectral slope value (in the $535\text{--}882\text{ nm}$ range) of -8 and $-4.3\%/100\text{ nm}$, respectively. These BS are sub-meter sized, with a dimension of $0.95\text{ m} \times 0.76\text{ m}$ for BS 486 and $0.76\text{ m} \times 0.56\text{ m}$ for the BS 487. The decrease in reflectance is not associated with image saturation, nor to local fast sublimation between the sequence color images (that last 230 s) because the order of acquisition of the filters was not in order of increasing wavelength. The sequence order was $649\text{--}535\text{--}480\text{--}360\text{--}700\text{--}882\text{--}989\text{ nm}$. Moreover, some BS survived several days, as shown in Fig. 8, excluding fast sublimation.

This peculiar spectral behavior was never reported in the existing literature in pre-perihelion BS, which were usually spectrally flat in the visible range. We observed only one pre-perihelion bright spot having negative slope, located in the Imhotep region (BS 42 in Table A.1), very likely related to frost because of its short lifetime (a few hours).

We attempted to estimate the water ice content of the Anhur blue bright patches using linear mixing model of the cometary dark terrain and water ice with different grain sizes, using the method detailed in Fornasier et al. (2016, 2019a):

$$R = p \times R_{\text{ice}} + (1 - p) \times R_{\text{DT}}. \quad (3)$$

Here R is the reflectance of the bright patches, R_{ice} and R_{DT} are respectively the reflectance of the water ice and of the cometary dark terrain, and p is the relative surface fraction of water ice.

Water ice spectra were produced using the Warren and Brandt (2008) optical constants and the Hapke radiative transfer

Table 2. Bright spots per region and spectral slope values.

Region	N_{tot}	N_{pre}	N_{perih}	N_{post}	Area _{tot} [m ²]	Slope _{pre} [%/(100 nm)]	Slope _{perih} [%/(100 nm)]	Slope _{post} [%/(100 nm)]
Aker	1	1	0	0	3	7.2	–	–
Anhur	86	5	8	73	9512	3.5±2.2	4.8±0.9	–0.7±0.5
Anubis	5	0	4	1	701	–	7.5±0.6	8.1
Anuket	30	24	1	5	1573	3.4±0.7	9.2	1.1±1.3
Apis	0	0	0	0	0	–	–	–
Ash	63	30	0	33	466	5.5±0.5	–	2.7±0.6
Aten	31	3	0	28	741	6.5±1.8	–	1.2±0.4
Atum	7	2	0	5	166	0.2	–	1.1±0.5
Babi	32	5	0	27	384	5.5±1.5	–	0.2±0.5
Bastet	7	3	0	4	30	6.1±0.6	–	–0.8±1.2
Bes	25	4	6	15	8158	3.4±1.4	8.7±1.1	2.1±0.8
Geb	4	4	0	0	86	8.1±1.2	–	–
Hapi	12	2	2	8	399	7.0	–	1.1±1.2
Hathor	4	0	0	4	81	–	–	0.3±1.3
Hatmehit	30	1	1	28	466	7.3	8.8	2.3±0.7
Imhotep	80	38	13	29	15714	4.8±0.5	6.4±0.8	1.9±0.8
Khepry	9	6	1	2	202	3.3±1.9	3.9	–1.1±4.1
Khonsu	61	10	5	46	5472	6.4±1.0	7.0±1.1	1.1±0.7
Ma'at	14	2	0	12	207	6.3±0.3	–	1.5±0.8
Maftet	6	5	0	1	22	7.6±0.6	–	3.6
Neith	2	2	0	0	48	5.2±0.30	–	–
Nut	2	0	0	2	7	–	–	5.9±0.2
Serqet	5	0	1	4	214	–	5.9	5.2±1.6
Seth	54	0	1	53	1197	–	10.4	0.3±0.4
Sobek	1	0	0	1	60	–	–	3.7
Wosret	31	3	1	27	805	5.6±1.4	9.2	–0.5±0.8

Notes. N_{tot} is the total number of bright spots per region identified, while N_{pre} , N_{perih} , and N_{post} are the BS observed pre-, during-, and post-perihelion, respectively. The average spectral slope values of the bright spots are reported for the three time frames, when at least one BS is observed, with the associated errors when available (i.e., when there are at least two BS per region).

model (Hapke 2002). To produce the absolute reflectance of the regions of interest, we applied the Hapke (2002) photometric model correction with parameters derived from Fornasier et al. (2016). However, we neglect the disk function correction, which is set to unity, because none of the shape models produced by the OSIRIS team has a spatial resolution high enough to correctly reproduce these tiny features. Considering this limitation, the estimated water ice abundance is about 20% for spot BS 489, and 75% for the brightest spot (BS 486). Conversely to most of the pre-perihelion BS observed with OSIRIS, which were matched by linear mixtures of the cometary dark terrain and water ice with grain sizes in the 30–100 μm range (Fornasier et al. 2016, 2021, 2019a; Oklay et al. 2017; O'Rourke et al. 2020), the ones analyzed here cannot be reproduced by water ice with relatively small grains. Even the BS showing a positive slope (BS 489, magenta square in Fig. 8) is better fitted by a model including water ice with large grains (1000 μm) than by the model including water ice with 100 μm grains. BS 487 is about five times brighter than the comet dark terrain, and its reflectance is reproduced by a mixture including 46% of water ice with large grains (3000 μm). Finally, BS 486 is 7–8 times brighter than the comet dark terrain (at 650 nm), and is dominated by water ice (75%) with very large grains (5000 μm , Fig. 8).

The fact that the BS spectrophotometry is reproduced by water ice with large grains in areal mixing with the cometary dark terrain is not unique, and was already reported for the

modeling of some bright patches in comet 67P observed with VIRTIS. In the infrared the spectra of the exposures of volatiles show the water ice absorption bands, permitting a deeper analysis of the composition and allows us to better constrain the components' physical parameters (grains size, temperature). Both Raponi et al. (2016) and Filacchione et al. (2016a) found that the compositional models reproducing the analyzed BS require the presence of both areal and intimate mixtures of the cometary dark terrain and water ice, this last having different grain sizes: a few tens of microns for the intimate mixture, and millimeter-sized grains for the areal mixture, as found in this paper for the tiny blue BS in Anhur (Fig. 8). The BS analyzed by Raponi et al. (2016) and Filacchione et al. (2016a) were detected pre-perihelion; they showed a positive spectral slope in the visible range, survived for 2–4 months with variable abundance of the water ice related both to the seasonal and diurnal cycle, and were observed in different regions. Unfortunately, infrared spectra of the negative sloped BS reported here are not available because the VIRTIS infrared channel has not been operational since May 2015. The presence of millimeter-sized grains in some water ice exposures of comet 67P may be due to the sintering of smaller water ice grains or to the growth of ice crystals produced by vapor diffused from the colder and water ice enriched material beneath the surface (Filacchione et al. 2016a).

However, water ice in comets is usually characterized by having small to medium grain size values: very fine grains (~ 1 –2 μm) were used to model the frost fronts in the Hapi region

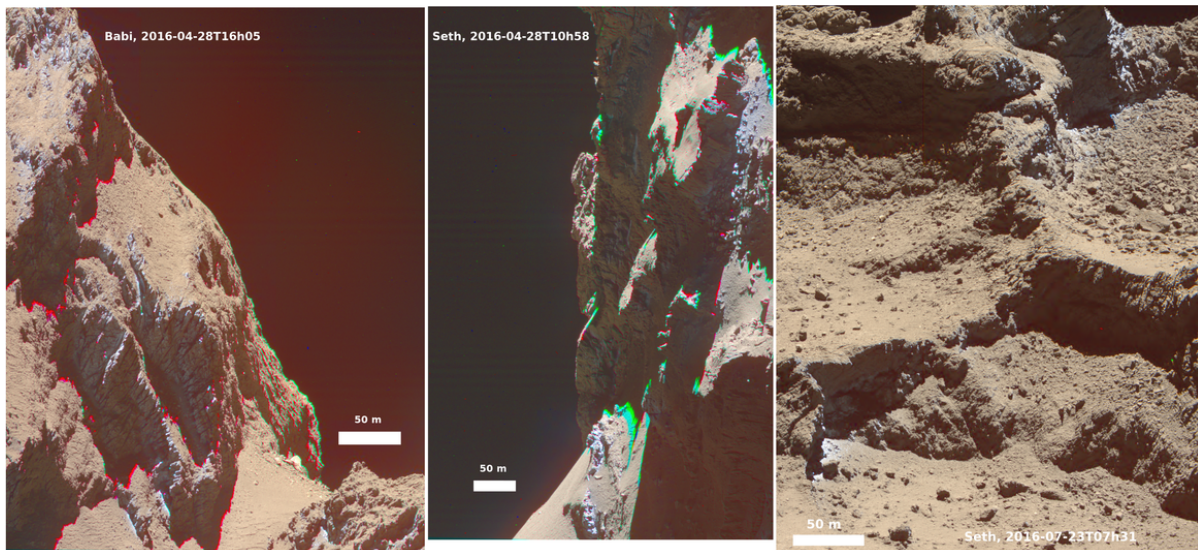


Fig. 9. Examples of RGB images showing frosts during the outbound orbit of comet 67P, near 3 au.

(De Sanctis et al. 2015), to model the overall decrease in the 67P nucleus spectral slope with the increasing activity approaching perihelion (Filacchione et al. 2016c; Ciarniello et al. 2016), to model the material excavated by the Deep Impact impactor on 9P/Tempel 1 (Sunshine et al. 2007), and were also found in the 103P/Hartley coma (Protopapa et al. 2014) and 17P/Holmes outbursts (Yang et al. 2009); coarser grains (30–100 μm) were used to model several BS of comet 67P (Filacchione et al. 2016a; Barucci et al. 2016; Pommerol et al. 2015; Fornasier et al. 2016; Oklay et al. 2017), and also on ice patches in comet 9P/Tempel 1 (Sunshine et al. 2006).

The high water ice abundance is not exclusive for the blue sloped BS reported in Fig. 8. In the literature high water ice abundances were reported for a few other BS (see Table A.1 for the BS numbers): over 80% in BS 480 (Hoang et al. 2020), 64–69.5% in BS 476 (Fornasier et al. 2021), and \sim 46% (O’Rourke et al. 2020) in the boulder onto which Philae impacted (BS 385), exposing primordial ice. All these BS, located in the Wosret region, should be fresh exposures of volatiles. Other BS in the Anhur region also have a large water ice fraction (30–40%), for example BS 461 (magenta symbol in Fig. 13, bottom panel, from Fornasier et al. 2019a), or the few large BS (1500 m^2 each) observed pre-perihelion in the Anhur-Bes boundary (Fornasier et al. 2016, BS 143 and BS 144). Oklay et al. (2017) reported long-lived BS in the Imhotep region, with estimated water ice content up to 48% in the feature called IF2.

Some of the post-perihelion blue spots may also be associated with frosts, especially those having short lifetimes. Frost was repeatedly observed in areas exiting from the cometary night or shadows, as shown in Fig. 9, and was already reported in the Anhur region (Fornasier et al. 2017, 2019a), near the final landing site Abydos (Hoang et al. 2020), and in Seth (Lucchetti et al. 2017), while it was less frequently observed pre-perihelion, with the notable exception of the Hapi region (De Sanctis et al. 2015).

6. Volatile exposures and cometary activity

Volatile exposures are directly linked to cometary activity. They may either be sources of jets or appear as the result of cometary

activity that generated self-cleaning and erosion of the nucleus, or they may be produced by morphological changes that expose the underlying volatile-rich materials.

Several relatively faint jets were observed directly departing from BS, as reported in Fornasier et al. (2019b), see, e.g., their Fig. 6), and some other BS appeared after cometary activity departing from their location or surroundings (Barucci et al. 2016; Deshapriya et al. 2016; Vincent et al. 2016; Fornasier et al. 2017).

Examples of self-cleaning of the comet are the two large bright patches reported by Fornasier et al. (2016, 2017) close to the Anhur-Bes regions boundary (BS 143 and 144 in Table A.1) that suddenly appeared in April–May 2015 in a smooth area. The ice survived exposed for about 7–10 days, and then these BS fully sublimated leaving a surface spectrally indistinguishable from the surrounding terrain. Notably, in the patch located within Anhur, the VIRTIS spectrometer detected in March 2015 for the very first time the exposure of carbon dioxide ice on a comet (Filacchione et al. 2016b). The discovery of carbon dioxide and water ices in this region demonstrates that different layers of volatiles are present within the nucleus, and points to compositional heterogeneity on large scales, on the order of tens of meters, on comet 67P (Fornasier et al. 2016).

Examples of ices exposed after activity and morphological changes are the following: the area rich in fresh water ice six times brighter than the surrounding dark terrain that appeared in the Aswan site after the cliff collapse observed on 10 July 2015, generated by an outburst, and that stayed exposed until at least the end of 2015 (Pajola et al. 2017a, BS168 in Table A.1); a $15 \times 5 \text{ m}^2$ bright patch formed inside a circular basin in Imhotep after an outburst on 3 July 2016 and that lasted for at least seven weeks (Agarwal et al. 2017, BS 485); a new scarp, 140 m long and 10 m high, formed in the Bes region, near the Anhur-Bes boundary and very close to BS 144 (where CO_2 ice was detected), exposing in the talus volatiles with water ice abundance estimated at $17 \pm 2\%$ (Fornasier et al. 2017); a second 10 m high scarp, located in the Anhur region, formed in January 2016 and showing at its base a surface of about 500 m^2 , brighter and bluer than the cometary dark terrain, exposing water ice for at least 5 months with estimated abundances of 26–30%

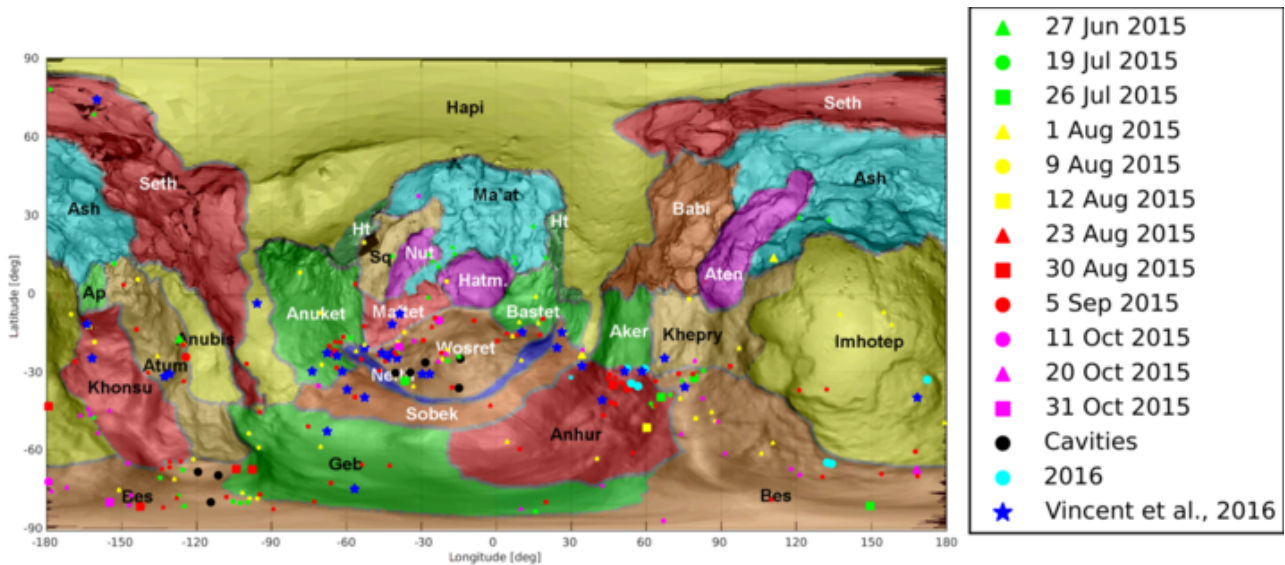


Fig. 10. Map with the sources of activity identified on the 67P nucleus in Vincent et al. (2016), blue asterisks, and Fornasier et al. (2019b).

(Fornasier et al. 2019a, BS 261); the appearance of a BS on a boulder in the Khonsu region at the beginning of January 2016, surviving for more than 6 months and associated with a cometary jet close to the perihelion passage (Deshapriya et al. 2018); again in the Khonsu region, a number of important morphological changes with dust removal up to 10 m in height and exposing several ice enriched patches (Hasselmann et al. 2019); water ice exposure in front of large expanding structures in Imhotep (Groussin et al. 2015, Deshapriya et al. 2018), observed shortly before the perihelion passage; the clustered features named CF2 and CF3 in Imhotep (Oklay et al. 2017), related to activity events and exposing water ice with abundances of $\sim 25\%$; the mechanical action of Philae that impacted into a boulder in the Wosret region, exposing fresh ice with abundance estimated at 46% (O'Rourke et al. 2020).

The comparison between Fig. 1, showing the BS distribution on the nucleus, and Fig. 10, displaying the sources of jets and outburst observed close to the perihelion passage, clearly indicates a correlation between activity and water ice exposures, in particular for the Anhur, Bes, Khepry, Imhotep, Khonsu, Atum, Anubis, and Anuket regions. As already noted in Fornasier et al. (2019b), activity events are correlated with local compositional heterogeneities (i.e., with local exposure of volatiles) and activated by solar illumination.

7. Size distribution of the volatiles exposures

We investigated the surface distribution of the volatile exposures. The area of the spots ranges from sub- m^2 , for example the spots observed on the Hatmehit rim in May 2016 (Hoang et al. 2020) or in Anhur (Fig. 8), to a few thousand square meters, like the two 1500 m^2 BS in the Anhur & Bes regions, observed in April–May 2015 (Fornasier et al. 2016), up to $\sim 5300 \text{ m}^2$ for the spot observed in Imhotep shortly after the perihelion passage (BS 188 in Table A.1).

Even if numerous bright spots are detected, the total surface of exposed water ice reported here (Table A.1) is $46\,714 \text{ m}^2$, which is 0.1% of the total 67P nucleus surface. This confirms that the surface of comet 67P is dominated by refractory dark terrains, while volatiles may occupy only a tiny areal fraction.

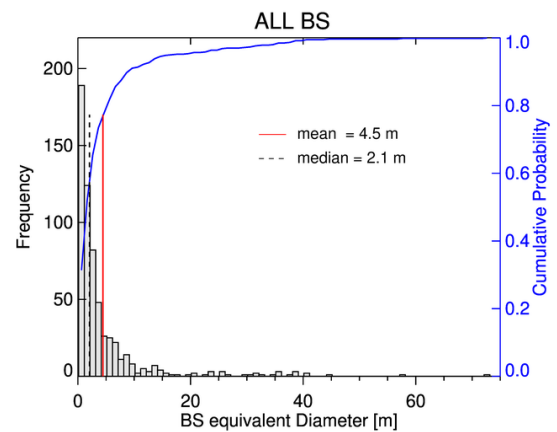


Fig. 11. Histogram density of the bright spot diameters identified on the 67P nucleus and reported in this study. Only those having diameter smaller than 80 m are represented, for clarity. The cumulative probability is shown in blue.

The majority of the volatile exposures are found in the regions of the big lobe. Their total area is about $42\,800 \text{ m}^2$, which correspond to 0.13% of the large lobe surface (31.66 km^2 , Thomas et al. 2018). The percentage of volatile exposures is six times smaller for the small lobe and the neck area, corresponding to 80 m for the Hapi and Sobek regions, with values of 0.02% (3450 m^2 over 17.26 km^2) and 0.016% (460 m^2 over 2.82 km^2), respectively.

The histogram showing the frequency of the BS diameter, estimated from the BS area assuming a square shape, is reported in Fig. 11. Bright spots are predominantly small; about one-third of them are smaller than 3 m^2 , and 170 are smaller than 1 m^2 .

Figure 12 shows the area distribution of the bright spots identified in the pre- and post-perihelion images (Table A.1), observed at resolutions higher than 1 px^{-1} , and having a surface lower than 10 m^2 ; because of the low resolution, we did not consider the observations close to the perihelion passage. Even if

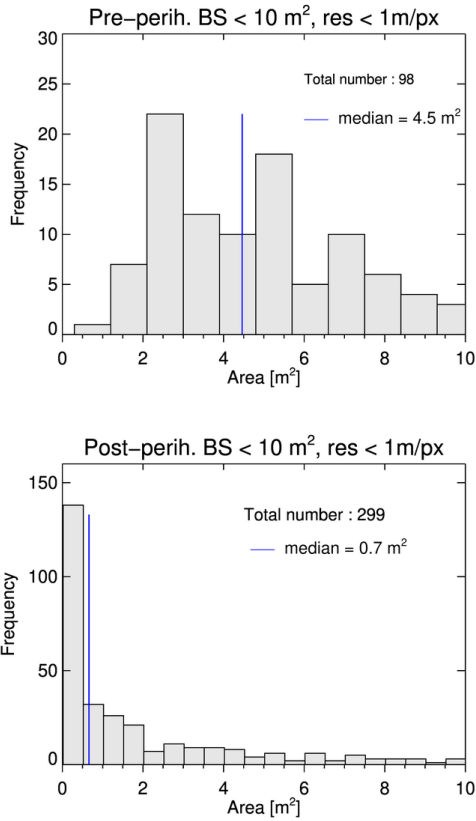


Fig. 12. Frequency of bright spot areas identified on the 67P nucleus for the pre-perihelion (top) and the post-perihelion (bottom) periods, observed at spatial resolution lower than 1 m px^{-1} .

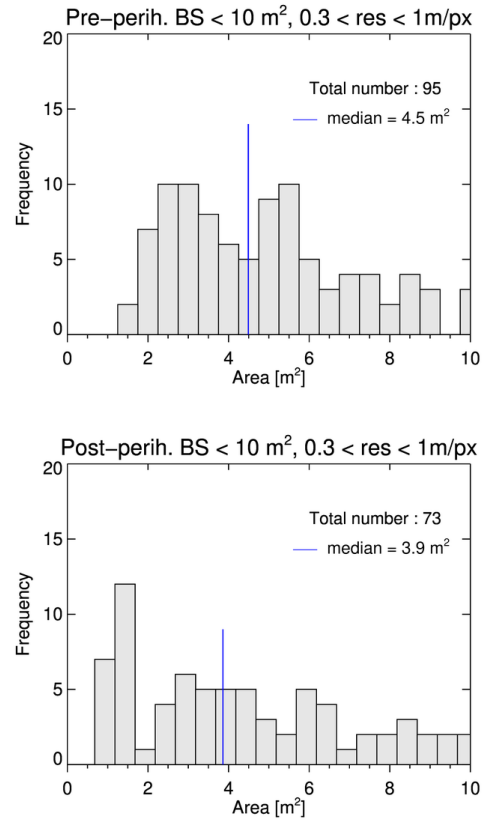


Fig. 13. Frequency of the bright spot areas identified on the 67P nucleus for the pre-perihelion (top) and the post-perihelion (bottom) periods, and observed at comparable high resolution ($0.33\text{--}1 \text{ m px}^{-1}$).

larger bright spots were present, we chose this limit in the analysis and to compute their surface mean values because in the pre- and post-perihelion data the great majority of these bright features have areas of a few square meters. With these criteria we count 98 pre-perihelion and 299 post-perihelion bright spots.

In addition to the different spectral slope distribution previously discussed, there is also a clear distinction in the areal distribution of the bright spots pre- and post-perihelion (Fig. 12). While pre-perihelion BS have a median surface of about 4.5 m^2 , in the post-perihelion images most of them are smaller than $1\text{--}2 \text{ m}^2$, with an average value of 0.7 m^2 , clearly indicating that high spatial resolution is mandatory to identify ice exposures on cometary surfaces.

The largest number of post-perihelion BS is clearly associated with an observational bias; approaching the end of the mission Rosetta went closer to the cometary surface achieving very high spatial resolution. More than one-third of the BS reported in Table A.1 (216 BS) were observed at a spatial resolution better than 0.33 m px^{-1} in post-perihelion images. When comparing the BS distribution pre- and post-perihelion observed at similar high resolution (i.e., between 0.33 m and 1 m px^{-1} ; Fig. 13), the average value of post-perihelion BS surface increases to 3.9 m^2 , and the distribution is more compatible with the one observed pre-perihelion, even if about one-fourth of the post-perihelion BS are relatively small ($<1.5 \text{ m}^2$). It should be noted that small BS are still not observed at a similar resolution in pre-perihelion images.

We also investigated the area distribution for the different cometary regions showing more frequently exposures of

volatiles. The regions having the higher number of BS (80–60) are located in the large lobe: Anhur, Imhotep, Ash, Khonsu, and Seth (Table 2), while Wosret and Hatmehit, with ~ 30 BS observed each, are the regions with more BS observed in the small lobe.

Our results on the bright spot dimensions support the findings of Ciarniello et al. (2022) and Fulle et al. (2020), who deduced that the bright spots on comets are exposure of the water ice enriched blocks (WEBs) forming, together with the refractory matrix, cometary nuclei, and whose dominant size is on the order of $0.5\text{--}1 \text{ m}$. WEBs should be formed of water ice-rich pebbles mixed with drier material, and exposed to the surface when the nucleus is eroded by the cometary activity. The fact that the majority of the bright spots are sub-meter sized is thus in agreement with these predictions and with the radar measurements the 67P comet provided by the Comet Nucleus Sounding Experiment by Radiowave Transmission (CONSERT), which indicate that the nucleus is homogeneous up to scales of a few meters (Ciarletti et al. 2017).

8. Duration and evolution of the bright spots

The lifetime of bright spots was estimated as the time in which a bright spot remains visible in different observing sequences, and thus it should be considered a minimum duration (Table A.1). This estimation is biased by the observing frequency-conditions; therefore, the real lifetime is usually longer than that reported here.

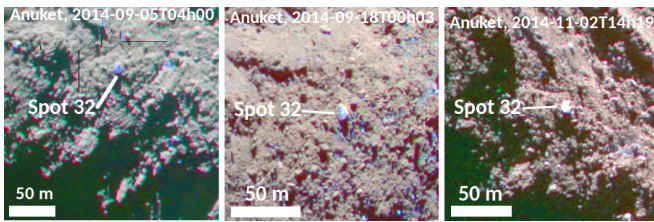


Fig. 14. Duration of BS 32 in Anuket region.

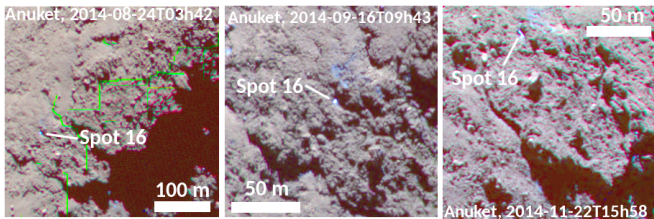


Fig. 15. Duration of BS 16 in Anuket region.

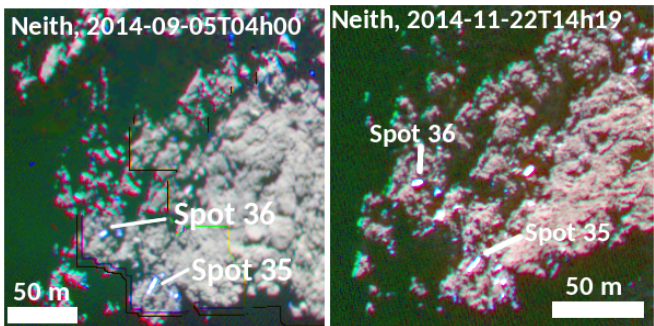


Fig. 16. Duration of BS 36 in Neith region.

Volatiles may survive exposed at the surface for a period varying from a few hours, in which case they are very likely frosts, to a few days and, for some of them, even to several months. A longer duration is usually found for water ice exposed after cliff collapse or the formation of new scarps, which may survive at the surface for several months, as detailed in the previous sections.

The evolution and water ice content of some clusters of BS was already reported in the literature, and it varies locally and with time: the CF1, CF2, and CF3 features in Imhotep contained spots with water ice fractions from 6.5% to 24.5% (Oklay et al. 2017); the water ice content of individual spots in the Hatmehit rim was estimated to be below 15% in late November and early December 2015, and exceeding 50% in late December 2015 and early 2016 (Hoang et al. 2020); joint OSIRIS and VIRTIS data analysis of BS indicates water ice abundances ranging from 0.1 to 7.2% (Barucci et al. 2016; Raponi et al. 2016), with seasonal variability during the BS lifetime (on the order of 2–4 months).

A few examples of BS duration are reported in Figs. 14–17. For pre-perihelion images, BS 32 and BS 16 in Anuket survive for at least 2 and 3 months, respectively (Figs. 14, and 15), and BS 35 and BS 36 in Neith for about 2 months (Fig. 16). An example of post-perihelion duration is reported for Atum, where BS 253 survived exposed at the surface for at least 84 days, and BS 204 for more than 4 months (Fig. 17).

Figure 18 shows the spectral slope value versus the duration for all the bright spots here reported, and for which the minimum duration was evaluated. Black points are post-perihelion

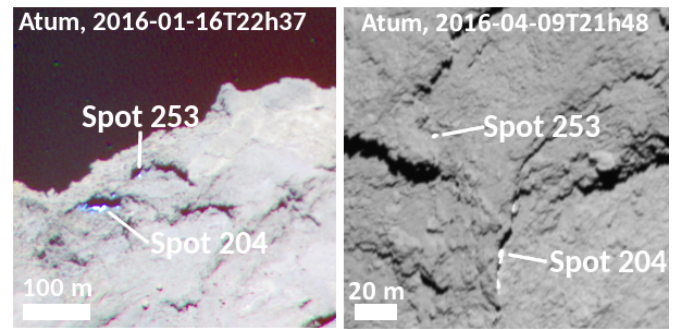


Fig. 17. Duration of BS 204 in Atum region.

BS, while red and blue points indicate the pre-perihelion observations, for the August 2014–January 2015, and February–May 2015 periods, respectively.

We separated the pre-perihelion observations into two datasets to investigate if any correlation exists between the blue spot color evolution and the overall evolution of the comet color and/or composition, due to the seasonal cycle of water, already observed and reported in the literature (Fornasier et al. 2016; Filacchione et al. 2016b; Ciarniello et al. 2022). The seasonal cycle of water produces on comet 67P, and very likely on comets in general, a bluing of the colors approaching perihelion, when the intense cometary activity erodes the nucleus exposing the underlying water ice enriched material. Models predict that between 20 and 70% of dust removed from the southern hemisphere (Keller et al. 2017; Hu et al. 2017; Fulle et al. 2021), which is illuminated for a short time but with high intensity during the perihelion passage, falls back in the northern hemisphere mainly in decimeter-sized dehydrated aggregate, relatively poor in water ice (Keller et al. 2017). For this reason, when the cometary activity decreases, the colors of the comet go back to red values because of the dehydrated dust blanket covering the nucleus. Already at 2.2 au outbound colors were reported to be as red as in pre-perihelion observations (Fornasier et al. 2016). A substantial bluing of comet 67P surface started since February 2015, according to Ciarniello et al. (2022). These authors predict that WEBs start to be exposed mostly from this period. Figure 18 shows that very few BS were observed in the February–May 2015 period. Most have short lifetimes of a few minutes to hours, and are very likely frosts. Instead, the two 1500 m² bright patches observed close to the Anhur–Bes boundaries (BS 143 and BS 144 in Table A.1) have a spectral slope close to zero, a water ice abundance up to 30%, and a lifetime of 1–2 weeks, and thus are very probably primitive WEB exposures. Long-lived BS show variable spectral slope values, with negative values observed predominantly in the post-perihelion period, as already described in Sect. 5.

To further constrain whether the BS exposed after February 2015 (inbound phase) and up to the post-perihelion phase can be interpreted in terms of primordial WEB exposures, the measured BS color (spectral slope) can be directly compared with the expected value for WEBs, as computed by spectral modeling following an approach similar to Ciarniello et al. (2022), based on Hapke’s theory (Hapke 2012)¹. WEBs are modeled as intimate

¹ In Ciarniello et al. (2022) the modeled quantity from which the color is inferred is the “effective single scattering albedo,” a proxy of the reflectance factor, while in the present work our computations refer to the reflectance factor itself, to be directly compared with OSIRIS observations.

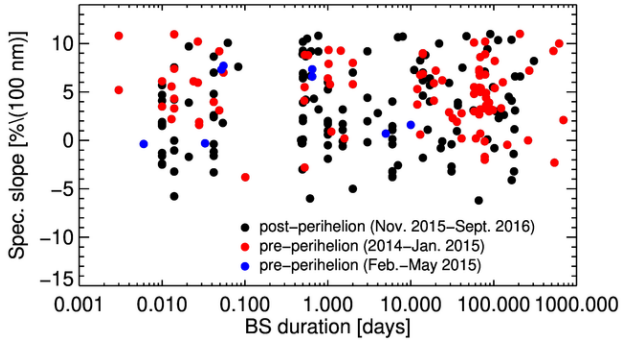


Fig. 18. Spectral slope value, evaluated in the 535–882 nm wavelength range, vs. BS duration.

mixtures of water ice and 67P dark terrain. For the dark terrain, we assume the optical properties (single scattering albedo and single particle phase function) estimated by Ciarniello et al. (2015) from VIRTIS observations (see also Ciarniello et al. 2022 for further details), while the single scattering albedo of water ice is computed from optical constants. To constrain the color, we compute the spectral slope from the simulated spectra as a function of the ratio of the reflectance factor at 882 nm and 535 nm, following the definition given in Sect. 2. VIRTIS data are affected by a calibration residue in the 800–1000 nm spectral interval (Ciarniello et al. 2015; Filacchione et al. 2016a), thus the estimated reflectance of the dark terrain at those wavelengths is likely underestimated. This would result in a slight underestimation of the modeled spectral slope, as it involves the computation of the reflectance factor at 882 nm. To bracket the correct spectral slope value, we then perform the computation also in the reduced interval 535–800 nm, where the dark terrain reflectance from VIRTIS observations is more reliable. Given the overall shape of the 67P spectrum, with a steeper slope shortward of 800 nm, this spectral slope value likely overestimates the expected value over the 535–882 nm interval.

In Table 3, we report the estimated spectral slope of different intimate mixtures of water ice and dark terrain with variable abundances. For completeness, we run simulations varying the water ice grain size (10, 100, 1000 μm), assuming this is the same as the dark material. In the model of Ciarniello et al. (2022) (hereafter WEB model), BS from WEB exposures are assumed to be characterized by a dust-to-ice mass ratio $\delta \approx 2$ (O’Rourke et al. 2020), and thus their predicted spectral slope would be on the order of $\approx 1.5\text{--}2.4\%/ (100\text{ nm})$ (Table 3). This is consistent with the average BS color during the post-perihelion phase and with the spectral slope of Anhur-Bes bright patches ($\approx 0.7\text{--}1.6\%/ (100\text{ nm})$) observed in April 2015, supporting the idea that such BS are exposures of original WEBs. The average BS color during the pre-perihelion phase, from observations carried out mostly before February 2015 ($\approx 4.9 \pm 0.3\%/ (100\text{ nm})$), is consistent with BS having $\delta \approx 8$, and thus likely does not represent the exposure of WEBs. The pre-perihelion BS color could also be possibly explained by BS undergoing partial self-cleaning (see Sect. 9).

It is difficult, however, to interpret the spectral slope in terms of dust-to-ice ratio because it depends on the spatial resolution, on the intrinsic water ice abundance in mixtures, on the water-ice grain size, and also on the spectral phase reddening. This last (i.e., the phenomenon related to the increase in colors and spectral slope values with increasing phase angle) is very important and is well characterized for the dark terrain (Fornasier

Table 3. Bright spot spectral slope (535–882 nm) as a function of the volumetric abundance and grain size of water ice mixed with 67P dark terrain; delta represents the dust-to-ice mass ratio.

Water ice vol. ab.	δ	Spec _{slope} (gs 10 μm)	Spec _{slope} (gs 100 μm)	Spec _{slope} (gs 1000 μm)
0.9	≈ 0.2	0.56 (0.81)	0.50 (0.78)	-0.055 (0.46)
0.8	0.5	0.83 (1.18)	0.79 (1.16)	0.40 (0.94)
0.5	2	1.78 (2.45)	1.75 (2.44)	1.52 (2.31)
0.3	≈ 4.7	2.95 (4.00)	2.93 (3.99)	2.75 (3.89)
0.2	8	4.11 (5.51)	4.10 (5.50)	3.95 (5.42)
0.1	18	6.66 (8.78)	6.64 (8.77)	6.5 (8.71)

Notes. Values in parentheses are computed over the interval 535–800 nm (see text). The optical properties of the dark terrain (single scattering phase function and single particle phase function) adopted in the modeling are assumed from Ciarniello et al. (2015, 2022) and do not depend on grain size. Three different water ice grain sizes (gs) are simulated: 10, 100, and 1000 μm . For each case volumetric abundances are defined assuming that water ice and dark terrain have the same grain size. For the purpose of this work, the spectral slope is computed at a reference observation geometry with incidence angle = 45° , emergence angle = 45° , and phase angle = 90° .

et al. 2015), but has not been determined for the bright spots because of their limited phase angle coverage coupled with their relatively short visibility.

9. Discussion

Figure 19 shows the BS duration versus their surface (Table A.1). It clearly demonstrates that the BS lifetimes are inconsistent with an explanation of all the observed BS in terms of diurnal or seasonal frost. The BS lifetimes do not depend on the heliocentric distance r_h : the largest range of lifetimes approaches six orders of magnitudes for BS all observed at $r_h > 3\text{ au}$, thus evidencing that the main factor driving the BS lifetime is its thickness. Since water-ice frost can be observed if its thickness is $T \geq 1\ \mu\text{m}$, the BS with the longest lifetimes would require $T \approx 1\text{ m}$, inconsistent with frost build-up by diurnal or seasonal thermal inversion below the nucleus surface (De Sanctis et al. 2015; Fornasier et al. 2016) or due to the condensation on the nucleus of water vapor from the coma.

Bright features due to diurnal frost have a lifetime shorter than the nucleus rotation period (12.4 h, Mottola et al. 2014) and form the lower cluster in Fig. 19, which is independent of the BS area, because diurnal frost occurs in sunrise nucleus shadows along the terminator, which may have any area. For instance, Fornasier et al. (2016) analyze color sequences close to the perihelion passage, and find frost fronts moving with the cometary morning shadows that have a permanence time of a few minutes and a solid ice equivalent thickness of 1.5–2.7 mm.

BS lasting more than 2 days form the upper cluster in Fig. 19, and are consistent with the WEB model (Ciarniello et al. 2022) (i.e., the proposed nucleus structural model is consistent with the observed seasonal evolution of the 67P nucleus color), which is based on the only available activity model consistent with dust ejection (Fulle et al. 2020). WEBs are blocks of sizes ranging from 0.5 to 1 m and composed of water-rich pebbles, embedded in a matrix of water-poor pebbles (Ciarniello et al. 2022). Water-rich pebbles have a refractory-to-water-ice mass ratio $\delta \approx 2$ (O’Rourke et al. 2020), whereas water-poor pebbles have $\delta \approx 50$ (Fulle et al. 2021). Water-rich pebbles probably formed at the

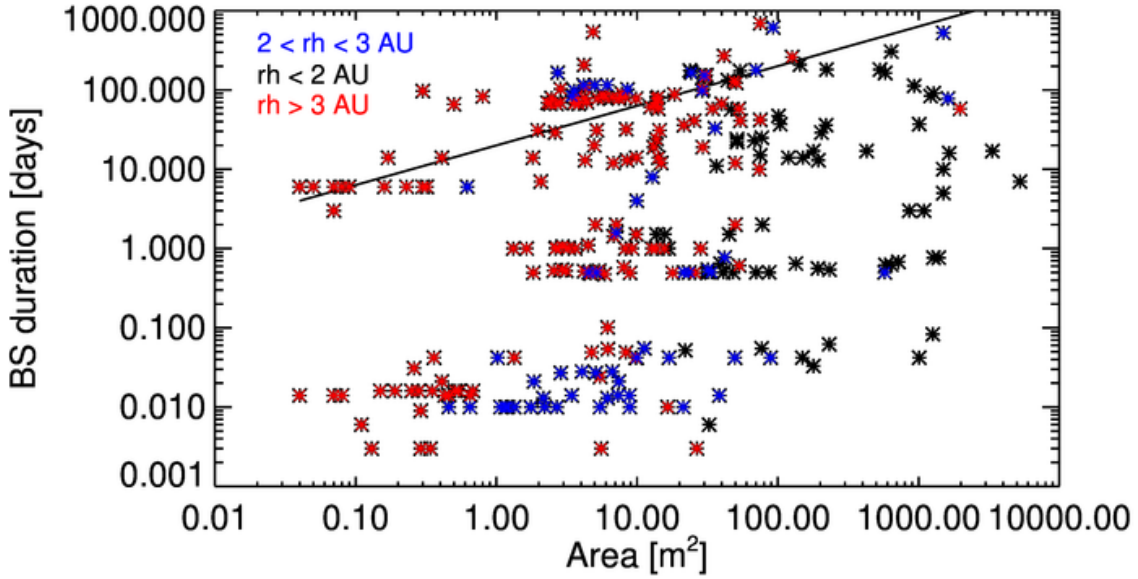


Fig. 19. BS duration vs. area distribution. The heliocentric distance of the 67P comet (r_h) is indicated using symbols with different colors. The black line represents the expected lifetime of bright spots predicted by the WEB model, assuming an erosion rate of 5 cm day^{-1} .

water-snow line of the protoplanetary disk due to the recondensation of water vapor (Fulle et al. 2021), so that their water ice is crystalline and may reach millimeter sizes, consistent with the extreme blue color of some BS (Fig. 8). Such millimeter-sized water ice is always embedded inside the dust particles composing all the centimeter-sized pebbles structuring every comet nucleus (Blum et al. 2017). Such a pebble structure is a necessary condition driving cometary activity (Fulle et al. 2020).

At $r_h = 3 \text{ au}$, the WEB model predicts a δ -independent nucleus erosion $E = 5 \text{ cm day}^{-1}$ (Fulle et al. 2020), best fitting the observed erosion during August–November 2014 in the Hapi deposits (Cambianica et al. 2020), which are composed of water-poor pebbles (Fulle et al. 2021). Therefore, the model predicts the same erosion also for all the BS lasting more than a few days listed in Table A.1, which are composed of water-rich pebbles. The line in Fig. 19 shows the observed BS lifetimes longer than 2 days compared to the BS lifetime predicted by the WEB model according to the computed erosion E , assuming that each BS is a WEB exposed by the ongoing nucleus erosion and of thickness $T = \sqrt{A}$, where A is the measured BS area (Table A.1). The predicted BS lifetimes best fit the available data for $0.1 \leq A \leq 10 \text{ m}^2$, with observed lifetimes longer and shorter by up of a factor ten than predicted, due to the fact that WEBs may have aspect ratios ranging from 0.1 to 10. WEBs of $T < \sqrt{A}$ have lifetimes shorter than predicted, the opposite if $T > \sqrt{A}$. On average, BS observed at $r_h < 3 \text{ au}$ show a shorter lifetime (Fig. 19), as predicted by the WEB model: $E = 13 \text{ cm day}^{-1}$ at 67P perihelion (Fulle et al. 2020).

For $A > 10 \text{ m}^2$, most BS have lifetimes shorter than predicted (Fig. 19); we recall that the duration reported here is a lower limit. This suggests that BS of $A > 10 \text{ m}^2$ are in fact clusters of BS of $A \leq 10 \text{ m}^2$ that appear as a single larger BS, due to the low resolution of the OSIRIS images. Most BS of $A > 10 \text{ m}^2$ have been observed at $r_h < 3 \text{ au}$ (Fig. 19), when Rosetta was farther from the nucleus than for $r_h > 3 \text{ au}$. We can conclude that the data shown in Fig. 19 constrain the average WEB cross section to $A \leq 10 \text{ m}^2$. The cross section distribution of all BS of $A \leq 10 \text{ m}^2$ shown in Fig. 12 constrains the median

WEB cross section to 0.7 m^2 , perfectly matching the WEB model (Ciarniello et al. 2022). A total BS area covering 0.1% of the nucleus surface is lower than the uncertainty affecting the BS aerial fraction consistent with the seasonal evolution of the nucleus color (Ciarniello et al. 2022). This is evidence that the observed BS are a few percent of the exposed WEBs driving the seasonal evolution of the nucleus color. This may be related to the fact that most OSIRIS images have a resolution insufficient to resolve exposed sub-meter WEBs, and/or related to the criteria here adopted to identify BS (i.e., having lower spectral slope values than the cometary dark terrain and higher reflectance). The average cometary dark terrain is a strong darkening agent in mixtures with ice, decreasing rapidly the BS reflectance. Thus, blue areas that are water ice enriched are often not as bright as the BS here reported (i.e., 50% brighter than the cometary dark terrain), and are therefore not included in this study.

Bright spots with lifetimes between 0.5 and 2 days form another area-independent cluster, which cannot be diurnal frost of lifetime longer than the nucleus rotation period. The most probable explanation of this cluster is the uniform fallout lasting at least the first three months of 2016, explaining the evolution of the dust backscattering observed in the 67P coma (Bertini et al. 2019), and most post-perihelion nucleus reddening (Ciarniello et al. 2022). Such uniform fallout is composed of water-poor decimeter-sized chunks eroded by the CO_2 -driven activity from the southern hemisphere during three months centered on the 67P perihelion (Fulle et al. 2021). If these chunks fall back on BS where the self-cleaning is occurring (Pajola et al. 2017b), then they are eroded into sub-chunk dust in about 2 days at the computed erosion rate of 5 cm day^{-1} (Fulle et al. 2020).

The self-cleaning BS are never buried by the fallout because the southern area is eroded at a perihelion rate of about 0.1 m day^{-1} and because the fallout is distributed over an area five times larger than the southern eroded area (Fulle et al. 2021), so that the first chunk monolayer would occur in about 5 days. On the other hand, most sub-chunk dust eroded by the self-cleaning falls back on non-self-cleaning BS, forming a dust monolayer in about 1 day (thus matching the average cluster lifetime shown

in Fig. 19) because self-cleaning and non-self-cleaning areas are similar (Fig. 19) and because the largest falling back dust is half the size of the parent chunks (Fulle et al. 2020). Close observations of dust deposits show that the self-cleaning areas are uniformly distributed among the non-self-cleaning areas, and that the non-self-cleaning deposits are much richer in sub-chunk dust than the self-cleaning deposits (Pajola et al. 2017b). Non-self-cleaning deposits may be composed of chunks of $\delta > 10^4$ (Ciarniello et al. 2022), thus preventing any water-driven erosion of the chunks themselves (Fulle et al. 2020). All of this explains why exposed WEBs form two different clusters in Fig. 19: the area-independent cluster which is fallout-driven and having a shorter lifetime than the area-dependent cluster, which is erosion driven.

10. Conclusions

We built the most extensive catalog of exposures of volatiles on comet 67P, based on OSIRIS-NAC color images, including 603 individual entries. We investigate the type, the spectral slope, the area distribution, and their minimum duration in a homogeneous way. Our main findings are the following:

1. Bright spots are found isolated or in clusters, with lifetimes ranging from a few minutes–hours, in which case they are very likely frost, to several days–months, in which case they should be considered exposure of original water ice enriched blocks.
2. Bright spots are more often observed post-perihelion and have typical sub-meter sizes, with a median value of 0.7 m^2 , indicating that high resolution is mandatory to observe icy exposures in comets.
3. The BS spectral slope evolved toward negative values in post-perihelion observations, indicating the presence of frost, for the short-lived ones, and of water ice with large grain sizes ($\geq 1000 \mu\text{m}$) for those having longer duration.
4. The BS lifetimes form three clusters (Fig. 19): (a) the area-independent cluster lasting less than 0.5 days, best explained by diurnal frost; (b) the area-independent cluster persisting from 0.5 to 2 days, best explained by a seasonal fallout lasting many months (Bertini et al. 2019, Ciarniello et al. 2022); and (c) the area-dependent cluster lasting more than 2 days, best explained by water-driven erosion of WEBs (Fulle et al. 2020, Ciarniello et al. 2022).
5. The observed erosion of BS lasting more than 2 days and of $\delta \approx 2$ matches the one observed in Hapi’s deposits of $\delta \approx 100$ (Cambianica et al. 2020). The erosion is therefore independent of the refractory-to-ice ratio, as predicted by the water-driven activity model (Fulle et al. 2020).
6. The observed BS lifetimes longer than 2 days are consistent with the predictions of the WEB model (Ciarniello et al. 2022).
7. The observed median of the BS cross section (0.7 m^2) fits that of the WEBs constrained by the seasonal evolution of the nucleus color (Ciarniello et al. 2022).
8. The observed evolution of the BS spectral slope matches the predictions of the WEB model. After February 2015, when the exposition of WEBs starts to make the average nucleus color bluer (Ciarniello et al. 2022; Fornasier et al. 2016), it has a value consistent with WEBs $\delta \approx 2$. Before this date it shows a redder color, probably due to partial self-cleaning of the few exposed WEBs.
9. The total integrated surface of volatile exposure is less than 50000 m^2 , which is less than 0.1% of the 67P nucleus

surface, indicating that the top layer of cometary nucleus composition (and the whole nucleus, according to the WEB model) is dominated by refractory material.

10. The majority of the BSs are observed in the large lobe of the comet, where they occupied 0.13% of the surface, while the small lobe has only 0.02% of volatile exposures. This finding supports the hypothesis of Massironi et al. (2015) on the binary structure of the comet, and the findings of El-Maarry et al. (2016) and Fornasier et al. (2021), on the fact that the small and large lobes of 67P comet have different mechanical and physical properties. Our study on volatile exposures highlights that the small lobe is pauperized in volatile abundance, at least in its upper layer, compared to the large lobe, even though it shows a seasonal evolution of colors (Ciarniello et al. 2022), driven by the exposure of WEBs, similar to the large lobe.

Acknowledgements. OSIRIS was built by a consortium led by the Max-Planck-Institut für Sonnensystemforschung, Goettingen, Germany, in collaboration with CISAS, University of Padova, Italy, the Laboratoire d’Astrophysique de Marseille, France, the Instituto de Astrofísica de Andalucía, CSIC, Granada, Spain, the Scientific Support Office of the European Space Agency, Noordwijk, The Netherlands, the Instituto Nacional de Técnica Aeroespacial, Madrid, Spain, the Universidad Politécnica de Madrid, Spain, the Department of Physics and Astronomy of Uppsala University, Sweden, and the Institut für Datentechnik und Kommunikationsnetze der Technischen Universität Braunschweig, Germany. The support of the national funding agencies of Germany (DLR), France (CNES), Italy (ASI), Spain (MEC), Sweden (SNSB), and the ESA Technical Directorate is gratefully acknowledged. We thank the Rosetta Science Ground Segment at ESAC, the Rosetta Mission Operations Centre at ESOC and the Rosetta Project at ESTEC for their outstanding work enabling the science return of the Rosetta Mission. We acknowledge the financial support from the France Agence Nationale de la Recherche (program Classy, ANR-17-CE31-0004). We thank the anonymous reviewer for his/her comments and suggestions which helped us to improve this article.

References

- Agarwal, J., Della Corte, V., Feldman, P. D., et al. 2017, *MNRAS*, **469**, S606
 Barucci, M. A., Filacchione, G., Fornasier, S., et al. 2016, *A&A*, **595**, A102
 Bertini, E. 2012, *ASP Conference Series*, **461**, 263
 Bertini, I., La Forgia, F., Fulle, M., et al. 2019, *MNRAS*, **482**, 2924
 Bibring, J. P., Langevin, Y., Carter, J., et al. 2015, *Science*, **349**, aab0671
 Biele, J., Ulamec, S., Maibaum, M., et al. 2015, *Science*, **349**, aaa9816
 Blum, J., Gundlach, B., Krause, M., et al. 2017, *MNRAS*, **469**, S755
 Cambianica, P., Fulle, M., Cremonese, G., et al. 2020, *A&A*, **636**, A91
 Capaccioni, F., Coradini, A., Filacchione, G., et al. 2015, *Science*, **347**, a0628
 Ciarletti, V., Herique, A., Lasue, J., et al. 2017, *MNRAS*, **469**, S805
 Ciarniello, M., Capaccioni, F., Filacchione, G., et al. 2015, *A&A*, **583**, A31
 Ciarniello, M., Raponi, A., Capaccioni, F., et al. 2016, *MNRAS*, **462**, S443
 Ciarniello, M., Fulle, M., Raponi, A., et al. 2022, *Nat. Astron.*, **6**, 546
 Davidsson, B. J. R., Sierks, H., Güttler, C., et al. 2016, *A&A*, **592**, A63
 De Sanctis, M. C., Capaccioni, F., Ciarniello, M., et al. 2015, *Nature*, **525**, 500
 Deshapriya, J. D. P., Barucci, M. A., Fornasier, S., et al. 2016, *MNRAS*, **462**, S274
 Deshapriya, J. D. P., Barucci, M. A., Fornasier, S., et al. 2018, *A&A*, **613**, A36
 El-Maarry, M. R., Thomas, N., Giacomini, L., et al. 2015, *A&A*, **583**, A26
 El-Maarry, M. R., Thomas, N., Gracia-Berna, A., et al. 2016, *A&A*, **593**, A110
 Filacchione, G., De Sanctis, M. C., Capaccioni, F., et al. 2016a, *Nature*, **529**, 368
 Filacchione, G., Raponi, A., Capaccioni, F., et al. 2016b, *Science*, **354**, 1563
 Filacchione, G., Capaccioni, F., Ciarniello, M., et al. 2016c, *Icarus*, **274**, 334
 Fornasier, S., Hasselmann, P. H., Barucci, M. A., et al. 2015, *A&A*, **583**, A30
 Fornasier, S., Mottola, S., Keller, H. U., et al. 2016, *Science*, **354**, 1566
 Fornasier, S., Feller, C., Lee, J.-C., et al. 2017, *MNRAS*, **469**, S93
 Fornasier, S., Feller, C., Hasselmann, P. H., et al. 2019a, *A&A*, **630**, A13
 Fornasier, S., Hoang, V. H., Hasselmann, P. H., et al. 2019b, *A&A*, **630**, A7
 Fornasier, S., Bourdelle de Micas, J., Hasselmann, P. H., et al. 2021, *A&A*, **653**, A132
 Fulle, M. 2021, *MNRAS*, **505**, 3112
 Fulle, M., Blum, J., Rotundi, A., et al. 2020, *MNRAS*, **493**, 4039
 Groussin, O., Sierks, H., Barbieri, C., et al. 2015, *A&A*, **583**, A36

- Hapke, B. 2002, *Icarus*, 157, 523
- Hapke, B. 2012, *Icarus*, 221, 1079
- Hasselmann, P. H., Barucci, M. A., Fornasier, S., et al. 2019, *A&A*, 630, A8
- Hoang, H.V., Fornasier, S., Quirico, E., et al. 2020, *MNRAS*, 498, 1221
- Hu, X., Shi, X., Sierks, H., et al. 2017, *MNRAS*, 469, S295
- Jorda, L., Gaskell, R., Capanna, C., et al. 2016, *Icarus*, 277, 257
- Keller, H. U., Barbieri, C., Lamy, P., et al. 2007, *Space Sci. Rev.*, 128, 433
- Keller H. U., Mottola, S., Hviid, S. F. et al. 2017, *MNRAS*, 469, S357
- La Forgia, F., Giacomini, L., Lazzarin, M., et al. 2015, *A&A*, 583, A41
- Lucchetti A., Pajola, M., Fornasier, S., et al. 2017, *MNRAS*, 469, S238
- Massironi, M., Simioni, E., Marzari, F., et al. 2015, *Nature*, 526, 402
- Mennella, A., Ciarniello, M., Raponi, A., et al. 2020, *ApJ*, 897, L37
- Mottola, S., Lowry, S., Snodgrass, C., et al. 2014, *A&A*, 569, A2
- Oklay, N., Mottola, S., Vincent, J.-B., et al. 2017, *MNRAS*, 469, S582
- O'Rourke, L., Heinisch, P., Blum, J., et al. 2020, *Nature*, 586, 697
- Pajola, M., Hofner, S., Vincent, J. B., et al. 2017a, *Nat. Astron.*, 1, 0092
- Pajola, M., Lucchetti, A., Fulle, M., et al. 2017b, *MNRAS*, 469, S636
- Poch, O., Istiqomah, I., Quirico, E., et al. 2020, *Science*, 367, aaw7462
- Pommerol, A., Thomas, N., El-Maarry, M. R., et al. 2015, *A&A*, 583, A25
- Protopapa, S., Sunshine, J. M., Feaga, L. M., et al. 2014, *Icarus*, 238, 191
- Quirico, E., Moroz, L. V., Schmitt, B., et al. 2016, *Icarus*, 272, 32
- Raponi, A., Ciarniello, M., Capaccioni, F., et al. 2016, *MNRAS*, 462, S476
- Raponi, A., Ciarniello, M., Capaccioni, F., et al. 2020, *Nat. Astron.*, 4, 500
- Sierks, H., Barbieri, C., Lamy, P. L., et al. 2015, *Science*, 347, aaa1044
- Sunshine, J. M., A'Hearn, M. F., Groussin, O., et al. 2006, *Science*, 311, 1453
- Sunshine, J. M., Groussin, O., Schultz, P. H., et al. 2007, *Icarus*, 190, 284
- Thomas, N., Sierks, H., Barbieri, C., et al. 2015, *Science*, 337, a0440
- Thomas, N., El Maarry, M. R., Theologou, P., et al. 2018, *Planet. Space Sci.*, 164, 19
- Tubiana, C., Güttler, C., Kovacs, G., et al. 2015, *A&A*, 583, A46
- Vincent, J.-B., Bodewits, D., Besse, S., et al. 2015, *Nature*, 523, 63
- Vincent, J.-B., A'Hearn, M. F., Lin, Z.-Y., et al. 2016, *MNRAS*, 462, S184
- Warren, S. G., & Brandt, R. E. 2008, *J. Geophys. Res.*, 113, D14220
- Yang, B., Jewitt, D., & Bus, S. J. 2009, *AJ*, 137, 4538

Appendix A: Supplementary material: Table**Table A.1.** List of the volatile exposure positions, types, and characteristics (slope, surface, duration) identified in this paper and in the literature.

BS #	Start Date	Type	Selected date	Lon (°)	Lat (°)	Region	Res (m px ⁻¹)	Area (m ²)	Slope	Duration	References
1	2014-08-03T05h21	4	2014-08-03T18h39	-178.89	-4.49	Imhotep	5.03	1973.03	10.1	58 days	P2015, O2017
6	2014-08-06T02h43	4	2014-09-05T02h35	-56.15	0.42	Anuket	0.81	25.44	0.2	41 days	P2015, D2018
7	2014-08-06T06h19	4	2014-09-03T03h44	115.99	14.60	Ash	1.24	41.45	7.2	269 days	O2017, Fi2016
16	2014-08-24T03h42	2	2014-09-16T09h43	-82.11	-19.79	Anuket	0.52	7.79	3.3	90 days	
22	2014-09-02T07h42	3	2014-09-15T05h42	-3.36	-8.12	Wosret	0.51	29.41	5.4	103 days	H2020
23	2014-09-02T07h42	3	2014-09-15T05h42	-3.50	-8.09	Wosret	0.51	2.86	8.2	103 days	H2020
24	2014-09-03T03h44	4	2014-09-16T03h10	116.93	13.63	Ash	0.51	14.1	4.9	81 days	O2017, Fi2016
25	2014-09-03T03h44	4	2014-09-16T03h10	118.78	14.55	Ash	0.51	6.67	4.4	81 days	O2017, Fi2016
26	2014-09-03T03h44	4	2014-09-15T01h40	115.69	13.43	Ash	0.52	8.25	3.6	81 days	O2017, Fi2016
27	2014-09-03T03h44	4	2014-09-14T00h05	118.45	12.69	Ash	0.54	5.91	3.6	81 days	O2017, Fi2016
28	2014-09-05T02h31	4	2014-09-05T02h31	-133.03	-21.04	Atum	0.81	12.46	0.2	61 days	B2016, D2018
29	2014-09-05T02h31	4	2014-09-05T02h31	-71.36	-30.00	Anuket	0.81	9.84	-0.1	78 days	
30	2014-09-05T02h31	4	2014-09-05T02h31	-67.46	-26.51	Anuket	0.81	13.77	-2.0	78 days	
31	2014-09-05T02h31	4	2014-09-05T02h31	-75.65	-29.70	Anuket	0.81	5.25	-1.7	78 days	
32	2014-09-05T02h31	3	2014-11-02T14h19	-72.00	-13.75	Anuket	0.6	52.81	3.0	58 days	
33	2014-09-05T02h35	2	2014-09-05T02h35	-62.26	-3.94	Anuket	0.81	8.48	0.6	13 days	
34	2014-09-05T02h35	2	2014-09-19T01h42	-60.14	-6.91	Anuket	0.52	4.27	6.76	13 days	
35	2014-09-05T04h00	2	2014-09-05T04h00	-59.63	-22.42	Neith	0.78	34.44	4.8	58 days	
36	2014-09-05T04h00	3	2014-09-05T04h00	-60.91	-22.16	Neith	0.78	14.14	5.5	58 days	
38	2014-09-05T05h21	4	2014-09-05T05h21	-171.84	-7.75	Imhotep	0.79	30.47	-0.46	146 days	B2016, D2018
39	2014-09-05T05h21	2	2014-09-05T05h21	-177.03	-21.45	Imhotep	0.79	75	2.1	694 days	O2017
47	2014-09-05T06h35	2	2014-09-19T06h34	174.20	-2.78	Imhotep	0.51	1.82	6.87	14 days	
55	2014-09-05T08h05	2	2014-09-05T08h05	138.21	33.69	Ash	0.77	8.94	2.8	-	
88	2014-09-18T00h33	4	2014-09-18T00h33	-65.10	-22.64	Anuket	0.52	5.14	3.5	-	
102	2014-11-02T14h19	3	2014-11-02T14h19	-70.79	-7.25	Anuket	0.6	4.25	6.7	-	
140	2015-04-13T04h47	2	2015-04-13T04h47	70.64	-33.28	Anhur	2.85	73.05	7.3	-	
141	2015-04-13T05h03	2	2015-04-13T05h11	67.42	-64.85	Anhur	2.85	32.53	-0.37	8 minutes	
142	2015-04-13T05h11	2	2015-04-13T05h35	60.14	-45.43	Anhur	2.85	178.92	-0.3	48 minutes	
143	2015-04-27T18h17	1	2015-05-02T08h53	66.8	-54.3	Anhur	2.32	1500	0.7	5 days	F2016, F2017
144	2015-04-27T18h17	1	2015-05-02T08h53	76.45	-54.15	Bes	2.32	1500	1.6	10 days	F2016, F2017
145	2015-05-02T05h53	2	2015-05-02T05h53	-141.8	-84.6	Bes	2.29	42.2	2.2	-	D2018
149	2015-05-16T08h38	1	2015-05-16T08h38	-18.87	21.62	Ma'at	2.37	39.2	6.59	15.53 hours	
168	2015-07-15T12h51	2	2015-07-15T12h51	-159.26	70.25	Seth	3.37	579.43	10.39	164 days	P2017
170	2015-07-19T03h36	1	2015-07-19T03h36	-99.72	-10.89	Hapi	3.38	227.9	6.86	-	
171	2015-07-26T07h48	1	2015-07-26T07h48	-118.97	-12.10	Anubis	3.17	151.09	6.2	14 days	
172	2015-07-26T07h48	1	2015-07-26T19h21	-123.68	-11.90	Anubis	3.15	119.02	7.0	14 days	
173	2015-07-26T09h18	2	2015-07-26T09h48	-162.94	-15.74	Khonsu	3.18	221.8	3.09	181 days	F2019
174	2015-07-26T11h40	2	2015-07-26T11h40	90.08	-44.93	Bes	3.17	531.56	6.6	181 days	
175	2015-07-26T11h40	1	2015-08-09T13h10	110.63	-28.88	Imhotep	5.76	3345.93	4.01	17 days	D2018
176	2015-07-26T11h40	1	2015-07-26T12h40	131.22	-35.01	Imhotep	3.15	427.65	6.4	17 days	
177	2015-07-26T11h40	1	2015-07-26T12h40	136.66	-21.52	Imhotep	3.15	179.02	5.7	17 days	
178	2015-08-01T07h38	2	2015-08-01T20h55	-132.93	-72.02	Bes	3.91	718.16	4.3	16.28 hours	
179	2015-08-01T11h51	2	2015-08-30T06h49	-119.10	-80.10	Bes	7.62	1278.73	10.98	91 days	F2019
180	2015-08-01T12h21	2	2015-08-30T06h49	-119.10	-68.70	Bes	7.62	929.99	10.35	113 days	F2019
190	2015-08-30T06h49	2	2015-08-30T07h29	57.29	-48.17	Anhur	7.62	1218.59	9.42	84 days	
192	2015-08-30T06h49	2	2015-08-30T11h41	-111.78	-80.89	Bes	7.61	1390.04	10.8	18.42 hours	
199	2015-11-22T21h13	2	2015-11-22T21h13	-70.87	-23.87	Anuket	2.38	96.16	-2.97	-	
204	2015-11-28T13h43	2	2016-01-16T22h37	-152.71	-1.46	Atum	1.61	44.15	2.63	133 days	
207	2015-11-28T15h04	2	2015-11-28T15h04	179.41	-5.37	Imhotep	2.42	41.02	6.53	12 hours	
251	2016-01-16T22h37	2	2016-01-16T22h37	-147.58	1.43	Atum	1.61	25.97	1.89	-	
252	2016-01-16T22h37	2	2016-01-16T22h37	-151.69	7.52	Atum	1.61	41.56	0.5	-	
253	2016-01-16T22h37	2	2016-04-09T21h48	-153.25	-2.60	Atum	0.51	3.44	0.1	84 days	
254	2016-01-17T02h29	2	2016-01-17T02h29	88.31	-3.35	Aten	1.6	102.41	-0.52	-	
255	2016-01-17T04h59	4	2016-04-28T16h05	58.98	4.61	Babi	0.34	8.56	-0.8	102 days	
261	2016-01-23T17h03	2	2016-04-23T19h14	46.05	-43.00	Anhur	0.52	30.07	4.5	152 days	
274	2016-02-27T08h29	2	2016-02-27T08h29	149.13	35.80	Ash	0.52	24.28	4.1	165 days	
275	2016-02-27T08h29	4	2016-08-10T16h05	149.04	36.14	Ash	0.2	2.73	-4.1	165 days	
287	2016-03-12T17h33	2	2016-03-12T17h33	150.30	35.47	Ash	0.3	3.58	5.5	150 days	
289	2016-03-12T17h48	2	2016-03-12T18h03	153.19	38.19	Ash	0.3	21.3	4.1	15 minutes	
370	2016-05-18T16h53	4	2016-05-18T16h53	112.28	27.22	Aten	0.16	14.44	-0.4	31 days	
371	2016-05-18T16h53	4	2016-05-18T16h53	112.07	27.33	Aten	0.16	5.18	-2.7	31 days	
372	2016-05-18T16h53	4	2016-05-18T16h53	116.78	30.11	Aten	0.16	0.83	-0.4	-	
373	2016-05-18T16h53	4	2016-05-18T16h53	116.51	28.64	Aten	0.16	1.97	-3.2	31 days	
374	2016-05-18T22h35	3	2016-05-18T22h35	-116.62	5.96	Seth	0.15	3.94	0.6	-	
375	2016-05-18T22h35	4	2016-05-18T22h35	-113.06	-1.82	Seth	0.15	2.67	-2.7	-	
376	2016-05-18T22h35	4	2016-05-18T22h35	-111.36	-2.66	Seth	0.15	1.27	2.09	-	
377	2016-05-18T22h35	4	2016-05-18T22h35	-112.54	-1.86	Seth	0.15	0.82	0.63	-	
378	2016-05-19T15h46	2	2016-05-19T15h46	166.4	-28.7	Imhotep	0.11	0.5	-6.2	66 days	D2018
385	2016-06-12T22h28	3	2016-06-14T10h29	-2.17	-7.66	Wosret	0.5	4.29	3.0	107 days	O2020
396	2016-06-16T09h54	2	2016-06-16T09h54	46.48	5.44	Babi	0.53	18.74	-3.2	-	
397	2016-06-16T09h54	2	2016-06-16T09h54	44.92	3.78	Babi	0.53	20.95	-3.2	-	
450	2016-06-25T01h37	2	2016-06-25T01h37	46.93	-44.11	Anhur	0.34	3.86	-3.3	-	
451	2016-06-25T01h37	2	2016-06-25T01h37	45.97	-43.92	Anhur	0.34	0.68	-2.15	-	
452	2016-06-25T01h37	2	2016-06-25T01h37	45.47	-47.01	Anhur	0.34	0.68	-6.34	-	
453	2016-06-25T01h37	2	2016-06-25T01h37	43.84	-51.07	Anhur	0.34	1.48	0.0	-	

Table A.1. continued.

BS #	Start Date	Type	Selected date	Lon (°)	Lat (°)	Region	Res (m px ⁻¹)	Area (m ²)	Slope	Duration	References
454	2016-06-25T01h37	2	2016-06-25T01h37	43.70	-54.46	Anhur	0.34	0.68	-5.52	–	
455	2016-06-25T01h37	2	2016-06-25T01h37	68.49	-60.56	Anhur	0.34	1.02	-1.3	–	
456	2016-06-25T06h09	2	2016-06-25T06h09	-164.3	-15.3	Khonsu	0.32	1.83	8.9	11.88 hours	H2019
457	2016-06-25T06h09	3	2016-06-25T06h09	-165.41	-12.92	Khonsu	0.32	7.2	9.27	–	
458	2016-06-25T06h09	2	2016-06-25T06h09	-160.61	-13.37	Khonsu	0.32	12.17	9.77	–	
459	2016-06-25T07h40	2	2016-06-25T07h40	166.04	-28.24	Imhotep	0.31	3.14	-5.6	–	
460	2016-06-25T11h50	2	2016-06-25T11h50	51.41	-43.96	Anhur	0.3	2.1	-2.4	–	
461	2016-06-25T11h50	2	2016-06-25T11h50	50.62	-44.61	Anhur	0.3	1.49	-0.6	–	
462	2016-06-25T11h50	2	2016-06-25T11h50	55.26	-51.14	Anhur	0.3	0.61	-3.53	–	
463	2016-06-25T11h50	2	2016-06-25T11h50	48.66	-46.07	Anhur	0.3	0.44	-1.39	–	
464	2016-06-25T11h50	2	2016-06-25T11h50	49.48	-45.89	Anhur	0.3	0.26	0.62	–	
465	2016-06-25T11h50	2	2016-06-25T11h50	45.51	-45.87	Anhur	0.3	0.35	-4.66	–	
466	2016-06-25T11h50	3	2016-06-25T11h50	46.14	-35.54	Anhur	0.3	0.35	-1.25	–	
467	2016-06-25T11h50	2	2016-06-25T11h50	59.36	-48.56	Anhur	0.3	2.45	5.7	–	
468	2016-06-25T11h50	2	2016-06-25T11h50	65.37	-45.94	Anhur	0.3	0.35	-0.98	–	
469	2016-06-25T11h50	2	2016-06-25T11h50	68.04	-56.83	Anhur	0.3	1.92	-2.5	–	
470	2016-06-25T19h24	3	2016-06-25T19h24	-172.95	-11.88	Imhotep	0.29	2.08	-3.9	–	
471	2016-06-25T19h24	3	2016-06-25T19h24	-172.43	-10.44	Imhotep	0.29	0.91	2.8	–	
472	2016-06-25T19h24	3	2016-06-25T19h24	-172.31	-9.84	Imhotep	0.29	2.66	-2.9	–	
473	2016-06-25T19h24	3	2016-06-25T19h24	-172.24	-15.33	Imhotep	0.29	3.57	1.1	–	
476	2016-07-02T15h22	2	2016-07-02T15h22	-25.56	-10.73	Wosret	0.27	1.2	-3.12	–	F2021
480	2016-07-09T15h03	2	2016-07-09T15h33	-2.72	-9.46	Wosret	0.23	1.34	-3.3	1 hour	H2020
485	2016-07-09T20h47	2	2016-07-24T10h13	172	-33.2	Imhotep	0.16	75	7.51	42 days	A2017
486	2016-07-16T15h03	2	2016-07-16T15h03	65.99	-50.11	Anhur	0.19	0.79	-8.0	–	
487	2016-07-16T15h03	3	2016-07-16T15h03	65.81	-50.05	Anhur	0.19	0.52	-4.3	–	
488	2016-07-16T15h03	2	2016-07-16T15h03	65.00	-50.10	Anhur	0.19	0.41	-1.8	14 days	
489	2016-07-16T15h03	2	2016-07-16T15h03	64.96	-50.11	Anhur	0.19	0.17	4.62	14 days	
490	2016-07-16T15h03	2	2016-07-16T15h03	64.77	-50.37	Anhur	0.19	0.35	-2.8	–	
491	2016-07-16T15h03	2	2016-07-30T05h09	64.87	-50.03	Anhur	0.17	0.17	-1.8	–	
492	2016-07-16T15h03	2	2016-07-16T15h03	69.93	-49.36	Anhur	0.19	1.07	5.5	–	
493	2016-07-16T15h03	2	2016-07-16T15h03	68.85	-58.20	Anhur	0.19	1.17	-1.7	–	
494	2016-07-16T15h03	2	2016-07-16T15h03	70.64	-57.93	Anhur	0.19	0.66	4.77	–	
495	2016-07-16T15h03	2	2016-07-16T15h03	68.30	-60.77	Anhur	0.19	0.52	-4.11	–	
496	2016-07-16T15h03	2	2016-07-16T15h03	66.41	-48.67	Anhur	0.19	0.41	-3.1	–	
497	2016-07-16T15h03	2	2016-07-16T15h03	66.38	-48.71	Anhur	0.19	0.24	-3.41	–	
498	2016-07-16T15h03	2	2016-07-16T15h03	63.72	-55.74	Anhur	0.19	1.11	-3.5	–	
499	2016-07-16T15h03	2	2016-07-16T15h03	63.73	-55.69	Anhur	0.19	0.21	-1.65	–	
500	2016-07-16T15h03	2	2016-07-16T15h03	67.90	-56.73	Anhur	0.19	0.55	-4.9	–	
501	2016-07-16T15h03	2	2016-07-16T15h03	67.76	-56.08	Anhur	0.19	0.35	2.1	–	
502	2016-07-30T05h09	2	2016-07-30T05h09	62.65	-46.20	Anhur	0.17	0.29	-6.5	–	
503	2016-07-30T05h09	2	2016-07-30T05h09	62.71	-46.12	Anhur	0.17	0.55	0.0	–	
504	2016-07-30T05h09	2	2016-07-30T05h09	62.89	-46.19	Anhur	0.17	0.2	-4.66	–	
505	2016-07-30T05h09	2	2016-07-30T05h09	63.05	-46.09	Anhur	0.17	0.12	1.58	–	
506	2016-07-30T05h09	2	2016-07-30T05h09	62.19	-47.30	Anhur	0.17	0.46	-2.7	–	
507	2016-07-30T05h09	2	2016-07-30T05h09	63.01	-47.82	Anhur	0.17	0.17	-2.45	–	
513	2016-08-10T16h05	4	2016-08-10T16h05	144.41	35.26	Ash	0.2	4.29	3.0	–	
514	2016-08-10T16h05	4	2016-08-10T16h05	146.22	36.52	Ash	0.2	8.47	2.7	–	
515	2016-08-10T16h05	4	2016-08-10T16h05	148.41	37.42	Ash	0.2	3.24	2.1	–	
542	2016-09-08T20h17	3	2016-09-08T20h17	48.59	-44.62	Anhur	0.08	0.64	-2.05	–	
543	2016-09-08T20h17	2	2016-09-08T20h17	52.68	-45.36	Anhur	0.08	0.47	-1.6	–	
544	2016-09-08T20h17	3	2016-09-08T20h17	49.67	-45.00	Anhur	0.08	0.17	3.6	–	
545	2016-09-08T20h17	2	2016-09-08T20h17	49.93	-44.92	Anhur	0.08	0.1	0.2	–	
546	2016-09-08T20h17	2	2016-09-08T20h17	53.51	-43.91	Anhur	0.08	0.12	3.1	–	
547	2016-09-08T20h17	2	2016-09-08T20h17	52.53	-45.21	Anhur	0.08	0.09	-0.93	–	
548	2016-09-08T20h17	2	2016-09-08T20h17	52.64	-44.52	Anhur	0.08	0.14	-3.9	–	
549	2016-09-08T20h17	2	2016-09-08T20h17	51.97	-45.16	Anhur	0.08	0.17	-2.8	–	
550	2016-09-08T20h17	2	2016-09-08T20h17	51.99	-45.40	Anhur	0.08	0.12	-1.94	–	
551	2016-09-08T20h17	2	2016-09-08T20h17	52.13	-45.94	Anhur	0.08	0.05	-3.77	–	
552	2016-09-08T20h17	2	2016-09-08T20h17	50.90	-46.56	Anhur	0.08	0.53	-4.4	–	
553	2016-09-08T20h17	2	2016-09-08T20h17	50.91	-46.53	Anhur	0.08	0.3	-7.4	–	
554	2016-09-08T20h17	2	2016-09-08T20h17	51.08	-46.25	Anhur	0.08	0.08	-5.62	–	
555	2016-09-08T20h17	2	2016-09-08T20h17	50.33	-46.30	Anhur	0.08	0.04	-5.92	–	
599	2016-09-23T15h57	2	2016-09-23T15h57	-159.20	-22.53	Khonsu	0.09	0.08	-3.22	20 minutes	
600	2016-09-23T15h57	2	2016-09-23T15h57	-157.53	-25.80	Khonsu	0.09	0.46	-1.04	20 minutes	
601	2016-09-23T15h57	2	2016-09-23T15h57	-158.84	-19.17	Khonsu	0.09	0.1	-3.61	–	
602	2016-09-23T16h17	2	2016-09-23T16h17	-159.73	-21.95	Khonsu	0.09	0.28	-4.81	–	
603	2016-09-24T00h57	3	2016-09-24T00h57	156.17	59.26	Ash	0.09	0.1	0.42	–	

Notes. Only some bright spots cited in the text are listed here, the full table with 603 entries is available at CDS. BS # is the bright spot number assigned here; Start date is the first time a bright spot was identified in the OSIRIS color sequences; Type represents the feature type according to the Deshapriya et al. (2018) classification scheme. Selected date is the date relative to the analysis of a given bright spot to determine its surface and spectral slope; Lon, Lat, and Region are the longitude, latitude, and 67P comet region name where a bright spot is found; Res corresponds to the resolution of the images acquired in the selected date; Area and slope are the BS surface and its spectral slope in the 535-882 nm range (evaluated in the selected date); Duration is the lifetime of bright spots when it was possible to estimate it. The majority of the BS were analyzed in the paper, but some were already presented in the literature and are referenced as follows: P2015: Pommerol et al. (2015); O2017: Oklay et al. (2017); D2018: Deshapriya et al. (2018); Fi2016: Filacchionet et al. (2016a); B2016: Barucci et al. (2016); H2019: Hasselmann et al. (2019); P2017: Pajola et al. (2017a); D2016: Deshapriya et al. (2016); H2020: Hoang et al. (2020); F2021: Fornasier et al. (2021); F2016: Fornasier et al. (2016); F2017: Fornasier et al. (2017); F2019: Fornasier et al. (2019a); O2020: O'Rourke et al. (2020); A2017: Agarwal et al. (2017).